Composites: Part A 152 (2022) 106683

Contents lists available at ScienceDirect

Composites Part A

journal homepage: www.elsevier.com/locate/compositesa

Numerical simulation on void formation and migration using Stokes-Brinkman coupling with effective dual-scale fibrous porous media

Jin Gang Lu [a,c], Sang Bok Lee [b], T. Staffan Lundström [c], Wook Ryol Hwang [d,*]

[a] School of Energy and Power Engineering, Jiangsu University, Zhenjiang 212013, China
[b] Composites Research Division, Korea Institute of Materials Science, Changwon 51508, Republic of Korea
[c] Division of Fluid and Experimental Mechanics, Luleå University of Technology, Luleå 97187, Sweden
[d] School of Mechanical and Aerospace Engineering, Gyeongsang National University, Jinju 52828, Republic of Korea

ARTICLE INFO

Keywords:
Optimal stokes-Brinkman coupling
Void formation and migration
Seepage flow
Void mobility
Liquid composite molding

ABSTRACT

Stokes-Brinkman coupling with the optimal characteristic parameters is applied to evaluate void formation and migration in effective dual-scale fibrous porous media during liquid composite molding. The optimal parameters, i.e., the effective viscosity in the continuous interfacial stress condition and stress jump coefficient in the stress jump condition, are accurately characterized. A series of multiphase flow simulations have been conducted to describe the evolutions of the void formation and its migration against the flow front position of the resin. We report that the voids are formed at low tow permeabilities and small aspect ratios of the fiber tow (relatively narrow channel). The distance between two fiber tows is observed to affect the number of voids formed. Voids immerged in resin subjected to a high permeability and a large surface tension yield a large mobility. Results from the particle tracing method reveal that in the case of high permeability and large surface tension, enhanced seepage flow adjacent to the flow front is formed because of the fountain flow nature and the bubble pushing mechanism, from which the voids in these cases migrate faster and therefore can easily escape from the resin.

1. Introduction

Liquid composite manufacturing (LCM) processes refer to the numerous techniques involved in manufacturing polymer composites based on resin injection through reinforcements [1]. LCM is widely applied in a large number of fields including aerospace, automobile, architecture, military and so on, owing to its remarkable advantages such as low injection pressure, relatively short cycle times, complex structure with a large scale, high efficiency and low pollution [2–4]. LCM processes include resin transfer molding (RTM) and vacuum assisted resin transfer molding (VARTM), which are the most common methods in manufacturing thermoset polymer composites [5]. In the process of RTM, the fiber reinforcement, also known as preform, is preplaced in a mold. Liquid resin is then injected to impregnate the preform and is cured to obtain a final solid part [6].

In RTM, the space between the fiber tows is on the scale of millimeters, whereas the space in-between individual fibers within the tow is in the order of microns, creating a dual-scale porous medium. Flows in the channel between adjacent tows (inter-tow flow) and those inside the fiber tow (intra-tow flow) are dominated by the pressure gradient, viscous forces, and capillary forces, respectively [7]. The competition between the inter- and intra-tow flow leads to the formation of voids by the hydrodynamic entrapment of air [8,9], which deteriorates the mechanical properties of the composite products [10–12]. Therefore, the main task becomes to minimize the presence of voids in the final part of the material. It has been reported that the vacuum application in air vents employed in VARTM can reduce the void content in the final product [13,14]. Besides, understanding the void formation mechanism as well as the effect of certain characteristic factors (e.g., processing parameters, resin and preform properties) on the void formation and its migration may play a key role in obtaining high-quality composite products with minimum void contents.

There have been extensive works reporting the void creation mechanisms or/and its migration during the LCM processes. For example, Vila et al. [7] conducted in-situ vacuum-assisted infiltration experiments using synchrotron X-ray computed tomography to study the mechanisms of microfluid flow within a fiber tow. They found that the fluid propagation at the microscopic level as well as the void transport mechanisms within the tow were related to the wetting between the fluid and fibers, the rheological properties of the fluid, and the local microstructure

* Corresponding author.
E-mail address: wrhwang@gnu.ac.kr (W.R. Hwang).

https://doi.org/10.1016/j.compositesa.2021.106683
Received 22 April 2021; Received in revised form 7 October 2021; Accepted 11 October 2021
Available online 19 October 2021

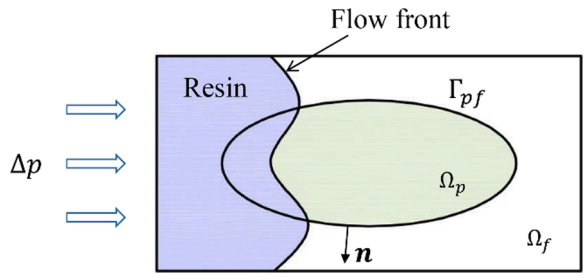

Fig. 1. Schematic description of the multi-phase flow with Stokes-Brinkman coupling. Subscript 'p' denotes the porous media while 'f' denotes the surrounding fluid. (For interpretation of the references to color in this figure legend, the reader is referred to the web version of this article.)

details (e.g., fiber volume fraction, fiber orientation) of the fiber tow. Hu et al. [10] developed a mathematical model to describe the void formation mechanism during RTM processes. The results showed that for a given fiber preform, the ratio of the weft axial permeability and warp permeability is responsible for the size of the void. Frishfelds et al. [11] modelled the motion of bubbles through inter-bundle channels in biaxial non-crimp fabrics using a permeability network model, bubble deformation criteria and a variety of analytical and probabilistic methods. It was found that paths of bubbles depend significantly on the position of the threads and the number of fibers crossing the inter-bundle channels. Shih and Lee [15] fabricated straight and confined micro-sized flow channels to visualize the void transport in LCM processes. It was reported that the mobility of the bubble is related to both the bubble size and wetting between fluid and solid surface. Gourichon et al. [16] proposed a numerical procedure to predict the dynamic void content in LCM by introducing critical pressure for void mobilization. They found that fast injection could lead to low global void content but very high local void content. Kang and Koelling [17] employed a transparent flow cell to visualize the void movement and deformation in the RTM process. Two critical capillary numbers determining the breakup and mobilization of drops have been provided. In addition to advective transport of voids, the air within the voids may dissolve into the resin [18].

The above-mentioned studies considered the effect of the realistic or quasi-realistic fibrous microstructure, when describing flows within the porous region, which may raise considerable difficulties in dealing with the dual-scale flow problems. For example, it may increase the computational cost remarkably for the numerical work. To simplify this, a model referred to as the 'representative porous region' with certain characteristic measures (e.g., permeability, porosity, etc.) was introduced to replace the actual porous microstructure [2,9,19–23]. With the Stokes equation (inter-tow flow) and the Darcy or Brinkman equation (intra-tow flow, i.e., flow in the representative porous region), the so called 'Stokes-Darcy' or 'Stokes-Brinkman' coupling can be utilized to evaluate the dual-scale flow in LCM processes. Brinkman's extension of Darcy's law is preferred mathematically and physically to the original Darcy's law in examining boundary layer effects [24]. In most cases, the effective viscosity in the Brinkman equation is considered to be the same as the fluid viscosity [2,9,20–22]. However, recently, it has been reported in the authors' previous work [24] that the optimal effective viscosity and the stress jump coefficient can be expressed in terms of the free interfacial geometry of the fibrous porous media.

In this work, Stokes-Brinkman coupling with optimal characteristic measures is applied to evaluate the void formation and migration in effective dual-scale fibrous porous media during the liquid composite molding. The optimal parameters, i.e., the effective viscosity in the continuous interfacial stress condition and stress jump coefficient in the stress jump condition, are accurately characterized. A series of two-dimensional multiphase simulations have been conducted to describe the evolutions of the void formation and its migration against the flow front position of the resin. The effects of the porous geometry (e.g., tow structure and permeability) and surface tension of the bubble on the void formation and its migration are also evaluated. It is worthwhile to mention that as the 2D simulation will not resolve the flow in the third (spanwise) direction, it will fail to describe the effect of the channel cross-sectional shape (e.g., circular, square, thin channel, etc.) on the bubble (void) formation and migration. Besides, it will also fail to capture the fully 3D behaviors of the bubble cross-sectional shape, deformation, break-up as well as the coalescence process [25]. However, in this work, the focus is set on the effect of the tow characteristics (e.g., permeability, interfacial stress boundary condition, tow geometry, etc.) on the bubble formation as well as on its mobility, without considering the detailed morphology of the bubble. Due to its low computation cost, the 2D simulation was introduced as an effective tool in the present work.

2. Modeling

We begin with the problem definition of the multiphase flow described by the Stokes-Brinkman coupling as shown in Fig. 1. A pressure-driven flow is defined to pass through a dual-scale domain Ω, which is composed of a fluid domain Ω_f and a porous domain Ω_p. The interface between the fluid and porous domains is denoted by Γ_{pf}, and $\boldsymbol{n}$ is the outward normal vector at the interface. Assuming the incompressibility is valid everywhere, the continuity equation is then

$$\nabla\cdot\boldsymbol{u} = 0, \tag{1}$$

where $\boldsymbol{u}$ is the velocity vector. Neglecting the inertia in such a small scale in this problem and any body forces like gravity, the flow in the fluid domain can be described by the Stokes equation

$$-\nabla p_f + \mu\nabla^2\boldsymbol{u}_f = 0. \tag{2}$$

The symbols p and μ denote the pressure and fluid dynamic viscosity, respectively. We employ the Brinkman equation to describe the flow in the porous domain as

$$-\nabla p_p + \mu_e\nabla^2\boldsymbol{u}_p - \frac{\mu}{K}\boldsymbol{u}_p = 0. \tag{3}$$

The symbols μ_e and K are the effective viscosity and permeability of the porous domain, respectively. By introducing a scalar parameter λ, which takes the value of zero in the fluid domain and one in the porous domain, the flow in the entire domain can then be described by a single equation: i.e., the Stokes-Brinkman coupling

$$-\nabla p + \mu\nabla^2\boldsymbol{u} + \lambda\left((\mu_e-\mu)\nabla^2\boldsymbol{u} - \frac{\mu}{K}\boldsymbol{u}\right) = 0. \tag{4}$$

The velocity continuity should be satisfied across the fluid/porous interface, while either a stress continuity or a stress jump boundary condition can be considered (see also in [24])

$$\boldsymbol{n}\cdot(\boldsymbol{\sigma}_p - \boldsymbol{\sigma}_f) = \begin{cases} \boldsymbol{0} & \text{continuous stress condition} \\ \left(\mu/\sqrt{K}\right)\boldsymbol{T}\cdot\boldsymbol{u} & \text{stress jump condition} \end{cases} \tag{5}$$

The symbols $\boldsymbol{\sigma}$ and $\boldsymbol{T}$ are the total stress tensor and stress jump tensor, respectively. In this work, we apply an isotropic tensor $\beta\boldsymbol{I}$ to replace the second order tensor $\boldsymbol{T}$ for simplicity, with β being the stress jump coefficient. It should be noted that, as suggested by Ochoa-Tapia and Whitaker [26] for the stress jump condition, the effective viscosity in the Brinkman equation is fixed as $\mu_e/\mu = 1/(1-\phi_s)$, with ϕ_s being the solid volume fraction, and the stress jump coefficient β remains as an adjustable parameter.

It would be worthwhile to briefly review the authors' previous work [24] on the estimation of the optimal choices of the effective viscosity in the continuous stress condition and the stress jump coefficient in the stress jump condition for the two-dimensional unidirectional fibrous porous media. For a simple pressure-driven flow over a flat porous surface with a top no-slip plate, the effective Navier-slip condition over

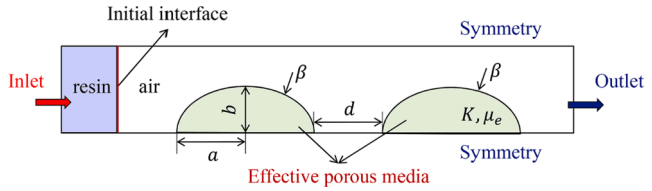

Fig. 2. Schematic description of resin/air two-phase flow through effective fiber tows using the Stokes-Brinkman coupling. (For interpretation of the references to color in this figure legend, the reader is referred to the web version of this article.)

an imaginary smooth interface between the fluid and porous media can describe the slip velocity as well as the velocity profile in the fluid domain accurately for various unidirectional porous architecture, even for anisotropic flows [27]. The slip velocity can be expressed in terms of the slip length b in the following manner

$$u_s = \frac{H/\sqrt{K}\cdot\left(H/\sqrt{K}+2\sqrt{K}/b\right)}{2\left(1+\sqrt{K}/b\cdot H/\sqrt{K}\right)}\cdot u_D, \tag{6}$$

here the symbols H and u_D are the height of the pure fluid channel and the Darcy velocity, respectively. In the authors' earlier work [27], we reported the slip length for various fibrous porous architecture and porosities, and interestingly, we showed that the slip length can be approximated by a single master equation independent of the porous architectures, once it is normalized and the dimensionless void length d^* is employed. The dimensionless void length denotes the fraction of the free surface at the interface and can be expressed as $d^* = 1-\sqrt{\phi_s/\phi_{smax}}$ with ϕ_{smax} being the maximum solid volume fraction in a unit cell ($\phi_{smax} = \pi/2\sqrt{3}$ in the hexagonal structure). Then, the dimensionless slip length b^* in the transverse direction, normalized by the fiber radius R, can be fitted by a single master equation as

$$b^* = 0.67{d^*}^{2.41} + 0.09, \quad b^* = b/R, \tag{7}$$

In the case of the Stokes-Brinkman coupling, based on the governing equation and the boundary conditions (see also the Eqs. (4) and (5) in the present work), one can readily obtain the solutions in the fluid region and porous region for the continuous stress condition and stress jump condition, respectively. Specifically, the slip velocity at the fluid/interface can be expressed in terms of the effective viscosity for the continuous stress condition [Eq. (8)] and in terms of the stress jump coefficient for the stress jump condition [Eq. (9)], respectively. Details can be found in [24],

$$u_s = \frac{H/\sqrt{K}\cdot\left(H/\sqrt{K}+2\sqrt{\mu_e/\mu}\right)}{2\left(1+\sqrt{\mu_e/\mu}\cdot H/\sqrt{K}\right)}\cdot u_D \quad \text{(Continuous stress)}, \tag{8}$$

$$u_s = \frac{H/\sqrt{K}\cdot\left(H/\sqrt{K}+2\sqrt{1/(1-\phi_s)}\right)}{2\left(1-\beta\cdot H/\sqrt{K}+\sqrt{1/(1-\phi_s)}\cdot H/\sqrt{K}\right)}\cdot u_D \quad \text{(Stress jump)}. \tag{9}$$

By comparing the slip velocity at the interface from the Navier-slip expression [Eq. (6)] with the effective slip length to the slip velocities subjected to the continuous/discontinuous stress conditions [Eqs. (8) and (9)], one can readily obtain the closed form expressions for the relative effective viscosity (normalized by the fluid viscosity μ_e/μ) and the stress jump coefficient (β) as follows

$$\frac{\mu_e}{\mu} = \frac{K}{b^2}, \tag{10}$$

$$\beta = \frac{\left(1/(1-\phi_s)-\sqrt{K}/b\right)\left(H^2/2K-1\right)}{H^2/2K+H/b}. \tag{11}$$

In the present work, we would like to employ these optimal parameters to evaluate the void formation and migration processes through a representative porous region. It is noted that the above procedures seeking for the optimal values of μ_e and β have been successfully extended to a porous medium composed of 3D spheres, details can be found in [28,29].

To track the evolution of the interface between the resin and air, the level-set method, which is commonly used in multiphase flow simulations, (for example, see Gangloff et al. [21,22], Hwang and Advani [30], and Frishfelds et al. [31]) is employed. The level-set function with the symbol ϕ is introduced to describe the different components of the fluid. The evolution of the interface is then governed by the convection equation of the level-set function

$$\frac{\partial\phi}{\partial t}+\boldsymbol{u}\cdot\nabla\phi = \gamma\nabla\cdot\left(\varepsilon\nabla\phi-\phi(1-\phi)\frac{\nabla\phi}{|\nabla\phi|}\right) \tag{12}$$

γ is the initialization parameter and ε is the interface thickness controlling parameter, which is usually set as $h_{\max}/2$, with $h_{\max}$ being the maximum size in the elements. To obtain a smooth phase distribution over the interface width, we apply a numerical smeared-out delta function

$$\delta(\phi) = \begin{cases} 6\phi(1-\phi) & 0<\phi<1 \\ 0 & \text{otherwise} \end{cases}. \tag{13}$$

A numerical Heaviside function $H(\phi)$ is then obtained by integrating the delta function over ϕ as

$$H(\phi) = \begin{cases} 0 & \phi = 0 \\ 3\phi^2-2\phi^3 & 0<\phi<1 \\ 1 & \phi = 1 \end{cases}. \tag{14}$$

With the Heaviside function in Eq. (14), for given fluids, e.g., the resin and air, the mixture viscosity can then be approximated as $\mu(\phi) = \mu_{\text{air}} + (\mu_{\text{resin}}-\mu_{\text{air}})\cdot H(\phi)$. It should be noted that, Eq. (14) implies that the resin/air interface is represented by the 0.5 level set ($\phi = 0.5$). Additionally, the effect of the interfacial tension between bubbles and resin is also considered by adding an additional source term $\boldsymbol{F}$ into Eq. (4). The interfacial tension force $\boldsymbol{F}$ can be expressed with the continuous surface stress model [32] as

$$\boldsymbol{F} = \nabla\cdot\left(\sigma\left(\boldsymbol{I}-\left(\boldsymbol{n}\boldsymbol{n}^T\right)\right)\delta(\phi)\right), \tag{15}$$

where σ is the surface tension coefficient. With the equations above and the applied pressure drop Δp at the inlet, the weak form of the present problem can be stated as follows: For $t>0$, find $u\in U, p\in P$ and $\phi\in\Phi$ such that

$$\int_\Omega q(\nabla\cdot u)d\Omega = 0, \tag{16}$$

$$\begin{aligned} -\int_\Omega p(\nabla\cdot v)d\Omega+\int_\Omega 2\mu(\boldsymbol{D}(\boldsymbol{u}):\boldsymbol{D}(\boldsymbol{v}))d\Omega+\int_\Omega 2\lambda(\mu_e-\mu)(\boldsymbol{D}(\boldsymbol{u}) \\ :\boldsymbol{D}(\boldsymbol{v}))d\Omega+\int_\Omega -\lambda\frac{\mu}{K}\boldsymbol{u}\cdot\boldsymbol{v}d\Omega \\ = -\sigma\int_\Omega\left(\left(\boldsymbol{I}-\left(\boldsymbol{n}\boldsymbol{n}^T\right)\right)\delta(\phi)\right) \\ :\boldsymbol{D}(\boldsymbol{v})d\Omega+\int_{\partial\Omega_{\text{inlet}}}\Delta p(\boldsymbol{n}\cdot\boldsymbol{v})d\Gamma \end{aligned} \tag{17}$$

$$\int_\Omega \Psi\cdot\left(\frac{\partial\phi}{\partial t}+\boldsymbol{u}\cdot\nabla\phi-\gamma\nabla\cdot\left(\varepsilon\nabla\phi-\phi(1-\phi)\frac{\nabla\phi}{|\nabla\phi|}\right)\right)d\Omega = 0 \tag{18}$$

for all $v\in\boldsymbol{U}, q\in P$ and $\Psi\in\Phi$.

Table 1
The schematic description of the hexagonal unit cell with the solid volume fraction, radius of the fiber, permeability and optimal effective viscosity for various unit cell widths.

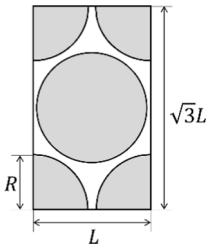

L [m]	ϕ_s	R [m]	K [m^2]	μ_e/μ
2×10^{-4}	0.1	3.32×10^{-5}	1.46×10^{-9}	11.246
1×10^{-4}	0.2	2.35×10^{-5}	1.73×10^{-10}	5.655
1×10^{-4}	0.5	3.71×10^{-5}	2.25×10^{-11}	1.227
1×10^{-4}	0.8	4.7×10^{-5}	5.43×10^{-13}	0.03
1×10^{-5}	0.8	4.7×10^{-6}	5.43×10^{-15}	0.03

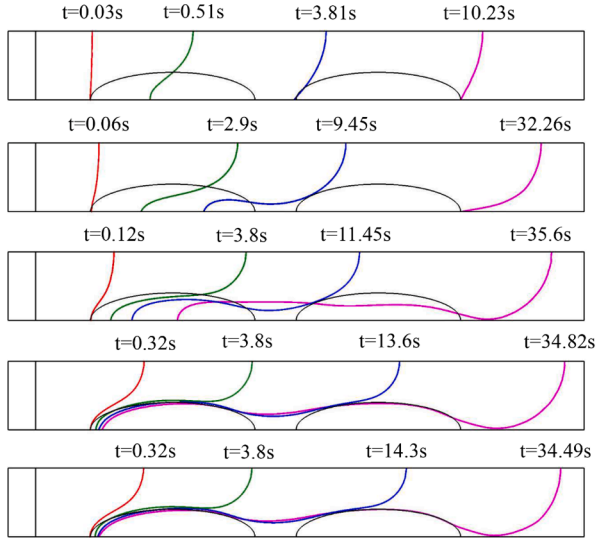

Fig. 3. The profiles of resin flow front ($\phi = 0.5$) at different stages for various tow permeabilities: (a) 1.46×10^{-9} m^2, (b) 1.73×10^{-10} m^2, (c) 2.25×10^{-11} m^2, (d) 5.43×10^{-13} m^2, (e) 5.43×10^{-15} m^2. (For interpretation of the references to color in this figure legend, the reader is referred to the web version of this article.)

3. Results and discussions

3.1. Void formation process

Fig. 2 shows the schematic description of the resin/air two-phase flow past two effective elliptic fiber tows. A pressure drop is assigned in the horizontal direction between the inlet ($p_{inlet} = 10$ Pa, left) and the outlet ($p_{outlet} = 0$ Pa, right). Two effective elliptic tows characterized by the permeability K and effective viscosity μ_e are initially placed in the air domain with the semi-major axis length a, semi-minor axis length b and tow distance d in-between. The bottom and top boundaries are considered symmetrical. The air phase (or void) is modeled as a fictitious incompressible fluid with the viscosity and density being 100 times smaller than those of the resin to avoid large magnitude differences in the final assembled stiffness matrix, whereas still be able to address the differences in physical behaviors of the air from that of the resin, see also [21,22,29]. The Stokes-Brinkman coupling (Eq. (4)) with either the continuous stress or stress jump conditions at the resin/porous interface is employed. Because of the larger flow resistance in the porous media, there appears to be a competition between the flow velocity in the pure fluid channel and that in the effective porous media. When the permeability is small enough, a void or dry spot is formed. In addition to the permeability, the geometric parameters of the fiber tows, e.g., the aspect ratio b/a and tow distance d/a may also affect the void formation. Therefore, in the remaining part of this section, the focus is set on the effect of these parameters on void formation. Note that the application of the effective elliptic tows (or the representative porous region) without any detailed information on the microstructure of the porous media implies that the capillary effect between the resin and porous media will be neglected in this work. In the Appendix section, one may find the strategy to incorporate the capillary pressure in our numerical framework as well as its effects on the process of both the bubble formation and migration. COMSOL Multiphysics 5.2 with the quadratic velocity, linear pressure interpolations, and linear level-set function is employed to implement the simulations. Even though not presented here, we tested the accuracy of the solution with the mesh refinement and checked for the good convergence of all the simulations.

We first evaluate the effect of the tow permeability on the void formation mechanism. It is assumed that the elliptic fiber tows are filled with equal-sized cylinders, which are packed as 'hexagonal' structures. The schematic description of the unit cell has been presented in Table 1. (One can also refer to the works of Lu et al. [27] and Gebart [33] for details.) The solid volume fractions ϕ_s are chosen as 0.1, 0.2, 0.5, and 0.8, respectively. The widths of the unit cell L are 0.2 mm, 0.1 mm, 0.1 mm, and 0.1 mm, respectively, with the Gebart's equation [33]

$$K = \frac{16}{9\pi\sqrt{6}}\left(\sqrt{\frac{\pi/2\sqrt{3}}{\phi_s}} - 1\right)^{5/2}\cdot R^2, \tag{19}$$

and the relationship between the solid volume fraction and radius of the cylinder, $\phi_s = 2\pi R^2/(\sqrt{3}L^2)$, the corresponding values of the radius are 0.0332 mm, 0.0235 mm, 0.0371 mm, and 0.047 mm, respectively. The tow permeabilities can thus be calculated as 1.46×10^{-9} m^2,1.73×10^{-10} m^2, 2.25×10^{-11} m^2, and 5.43×10^{-13} m^2, respectively. In this case, the continuous stress condition with the optimal effective viscosity is applied to implement the two-phase flow simulations using the Stokes-Brinkman coupling. The optimal choices of the effective viscosity can be determined using Eqs. (7) and (10) such that

$$\frac{\mu_e}{\mu} = \left(\left(0.67\left(1 - \sqrt{\phi_s/\left(\pi/2\sqrt{3}\right)}\right)\right) + 0.09\right)\cdot\frac{K}{R^2}, \tag{20}$$

which are 11.246, 5.655, 1.227, and 0.03, respectively. To check the cases with very low permeability on the void formation process, the width of the unit cell L has been decreased to 0.01 mm, while the solid volume fraction was kept the same value, $\phi_s = 0.8$. The corresponding radius of the cylinder and permeabilities are 0.0047 mm and 5.43×10^{-15} m^2, respectively. It is noted that even though the unit cell width along with the cylinder radius changes, the effective viscosity will not change, because it scales only with the solid volume fraction, according to Eqs. (19) and (20). The values of solid volume fraction, fiber radius, permeability and effective viscosity in this case for various unit cell widths have been also listed in Table 1. Fig. 3 shows the profiles of the resin flow front ($\phi = 0.5$) from the initial state to the state when the flow front leaves the second tow for various tow permeabilities. As expected, the flow resistance in the porous media increases, as the tow permeability decreases, and the time to reach a similar resin front location increases. For example, from the initial to the present state, the elapsed time values are 10.23 s, 32.26 s, 35.6 s, 34.82 s, and 34.49 s, respectively, as shown in Fig. 3(a) - (e). In the case of larger permeabilities (Fig. 3(a)-(b)), the differences in the resin velocity in the channel and that in the tow are not apparent, resulting in a non-distorted shape of the flow front and no voids can be detected. However, when the tow permeability is small enough (Fig. 3(c)-(e)), the resin in the channel moves significantly faster than that in the tow, heavily distorting the shape of the resin flow front and therefore voids are formed. In the case of very low permeabilities (e.g., Fig. 3(d)-(e)), there are no apparent

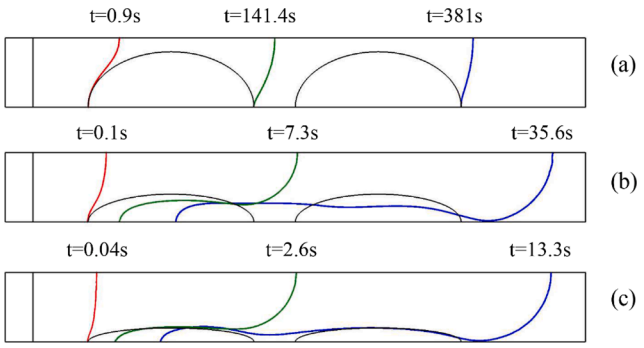

Fig. 4. The profiles of resin flow front ($\phi = 0.5$) at different stages for various aspect ratios: (a) $b/a = 2/3$, (b) $b/a = 1/3$, (c) $b/a = 1/6$. These three cases possess the same permeability ($K = 2.25 \times 10^{-11}$ m^2) and the tow distance ($d/a = 1/2$). (For interpretation of the references to color in this figure legend, the reader is referred to the web version of this article.)

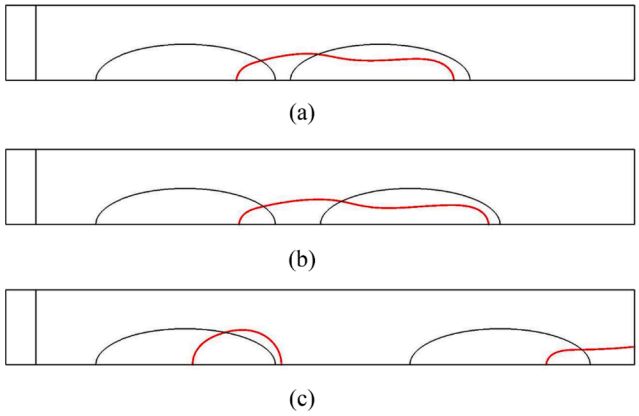

Fig. 5. The profiles of resin flow front ($\phi = 0.5$) for various tow distances: (a) $d/a = 1/6$, (b) $d/a = 1/2$, (c) $d/a = 3/2$. These three cases possess the same permeability ($K = 2.25 \times 10^{-11}$ m^2) and the aspect ratio ($b/a = 1/3$). (For interpretation of the references to color in this figure legend, the reader is referred to the web version of this article.)

differences of the flow front profiles at each stage.

Subsequently, the effect of two geometric parameters on the void formation mechanism is studied (i.e., the aspect ratio of the fiber tow b/a and tow distance d/a, see Fig. 2). As shown in Fig. 4(a) – (c), the aspect ratios b/a are 2/3, 1/3, and 1/6, respectively, with the same semi-major axis length a. The tow permeability is $K = 2.25 \times 10^{-11}$ m^2 in all the three cases. With a high aspect ratio, the pure fluid channel becomes narrower (Fig. 4(a)), leading to a blockage of the channel. Thus, resin in the channel is decelerated, yielding the resin velocity in the channel comparable with that in the tows. The profile of the flow front was found undistorted, and consequently, no voids have been created. However, for low aspect ratios (Fig. 4(b) and (c)), the resin velocities in the channel are significantly higher than those in the tows owing to the spacious pure fluid channel; therefore, voids are formed. Additionally, as expected, the consuming time also varies significantly with the aspect ratio to reach a similar state as shown in Fig. 4: from Fig. 4(a) to (c), the consuming time values are 381 s, 35.6 s, and 13.3 s, respectively.

Fig. 5 shows the resin flow front for various tow distances, i.e., (a) $d/a = 1/6$, (b) $d/a = 1/2$, and (c) $d/a = 3/2$. It should be noted that in these three cases, tows possess the same permeability ($K = 2.25 \times 10^{-11}$ m^2) with the aspect ratio ($b/a = 1/3$). From Fig. 5, it can be observed that in the case of a small tow distance (Fig. 5(a) and (b)), in which the two tows are located closely, the resin touches and infiltrates the second tow without fully filling in the gap between the two tows, forming only one void. However, when the tow distance is large enough (Fig. 5(c)), before reaching the second tow, the resin first fills in the gap between the two tows, leaving the first void to be trapped by the resin within the first tow. As the resin infiltrates the second tow, additional voids are formed. Hence, the tow distance may determine the number of voids formed in the final state.

Before closing this section, an arbitrary case is chosen to evaluate the effect of the stress boundary conditions applied at the fluid/tow interface on the void formation mechanism. The tow permeability K is given as 2.25×10^{-11} m^2. The aspect ratio (b/a) and tow distance (d/a) are 1/3 and 1/2, respectively. In the case of the continuous stress condition, both the identical ($\mu_e/\mu = 1$) and optimal ($\mu_e/\mu = 0.03$ in this case) effective viscosities are considered. In the case of the stress jump condition, the optimal stress jump coefficient can be obtained from Eq. (11) (see also [24]), which is found to be 4.83. The profiles of resin flow front from the initial state to $t = 7.89$ s with various interfacial stress conditions have been presented in Fig. 6. It can be observed that the resin migrates at different speeds with different interfacial stress conditions: in the continuous stress condition with the identical effective viscosity, the resin moves fastest, whereas it moves slowest with the optimal one.

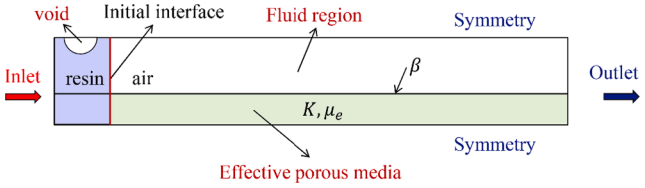

Fig. 7. Schematic description of a void transport in resin channel bounded by an effective porous wall using Stokes-Brinkman coupling. (For interpretation of the references to color in this figure legend, the reader is referred to the web version of this article.)

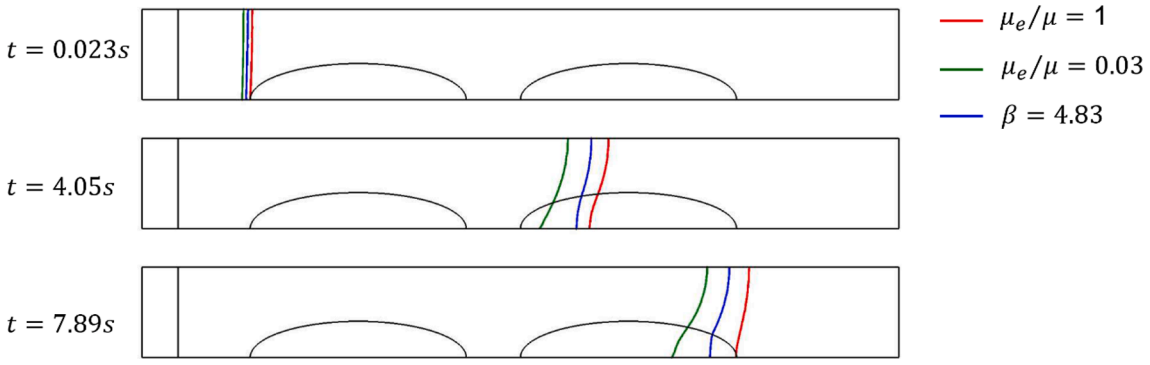

Fig. 6. The profiles of resin flow front at three different stages for various stress boundary conditions at the fluid/porous interface. (For interpretation of the references to color in this figure legend, the reader is referred to the web version of this article.)

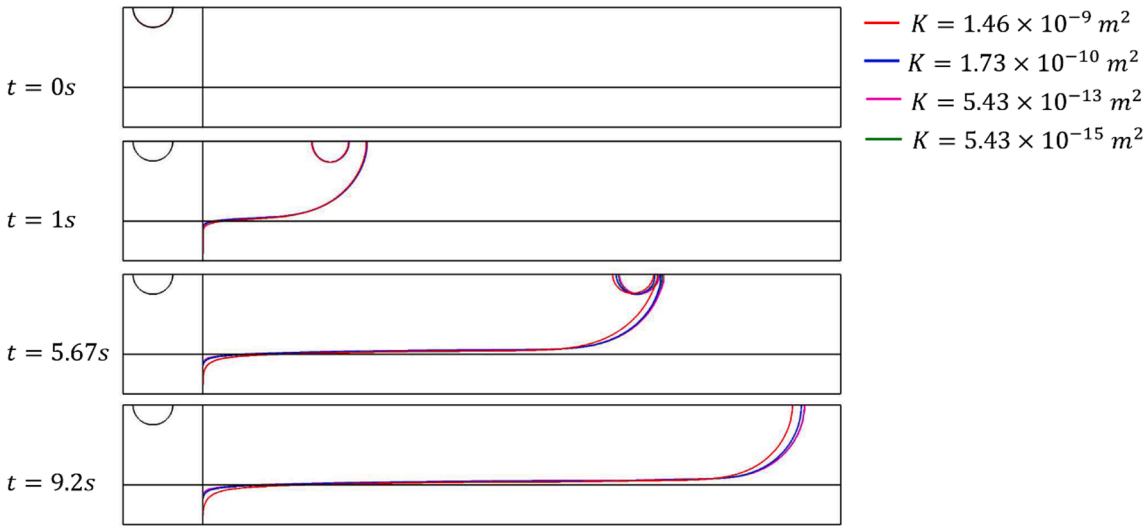

Fig. 8. Void evolution as well as profiles of resin flow front at different moments for various permeabilities. (For interpretation of the references to color in this figure legend, the reader is referred to the web version of this article.)

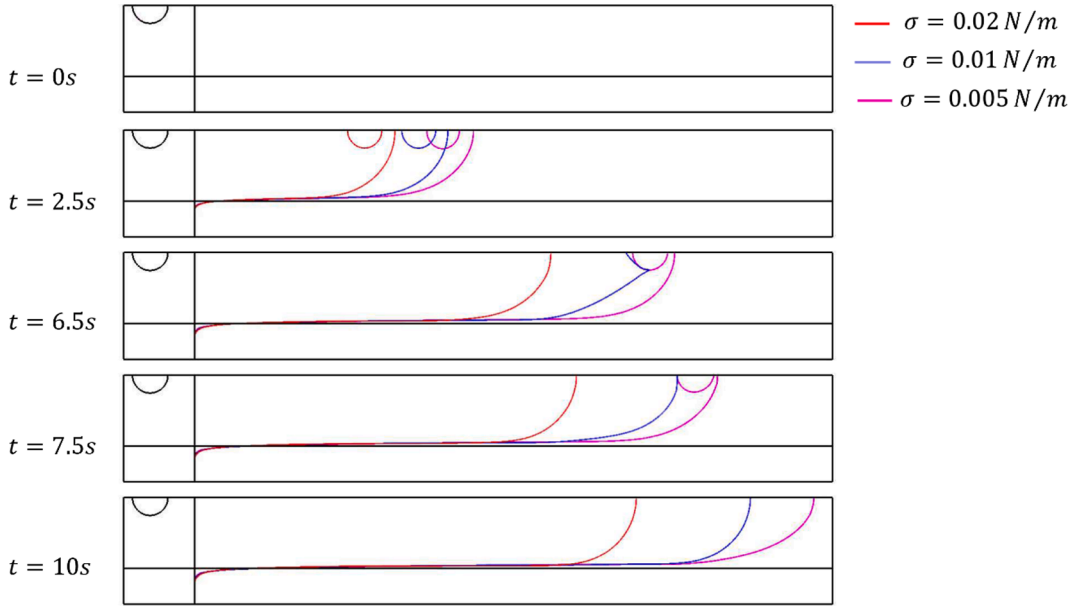

Fig. 9. Void evolution as well as profiles of resin flow front at different times for various surface tension coefficients.

The authors' earlier work [24] indicated that, under different interfacial stress boundary conditions (e.g., continuous or discontinuous), the velocity profile within the porous media varies each other especially in the boundary layer. As there is no corresponding experimental data available, it is difficult to draw conclusions that which stress condition yields the best behavior in predicting the resin migration. This issue will be addressed in our future work.

3.2. Void migration process

In this section, we explore the migration process of a void immerged in a resin channel bounded by an effective permeable wall with two characteristic parameters, i.e., the permeability K and effective viscosity μ_e. As shown in Fig. 7, a pressure drop is assigned in the horizontal direction between the inlet ($p_{inlet} = 10$ Pa, left) and the outlet ($p_{outlet} = 0$ Pa, right). The top and bottom walls are subjected to the symmetry boundary condition. As dragged by the resin, the void is expected to move with the resin, creating a race between the void and resin flow front. The goal of this simulation is to identify the effect of certain parameters, for example, the tow permeability K and surface tension coefficient σ, on the void migration process and the capability of voids to escape from the resin. By choosing the optimal effective viscosities (Section 2), the Stokes-Brinkman coupling with the continuous stress boundary condition is applied to solve this problem. COMSOL Multiphysics 5.2 was employed to implement the simulations and the mesh refinement has been conducted, though not presented here.

First, the effect of the porous permeability on the void migration process is scrutinized. As listed in Table 1, four different permeabilities of the effective porous media are considered, i.e., $K = 1.46 \times 10^{-9}$ m^2, 1.73×10^{-10} m^2, 5.43×10^{-13} m^2, and 5.43×10^{-15} m^2. The corresponding optimal effective viscosities are $\mu_e/\mu = 11.246$, 5.655, 0.03, and 0.03, respectively. Evolutions of the void as well as the resin flow front position at different moments are recorded in Fig. 8. It can be observed that in the case of large permeability (e.g., $K = 1.46 \times 10^{-9}$ m^2), the resin flow front in the channel migrates slower than those subjected to small permeabilities. Because the amount of impregnated

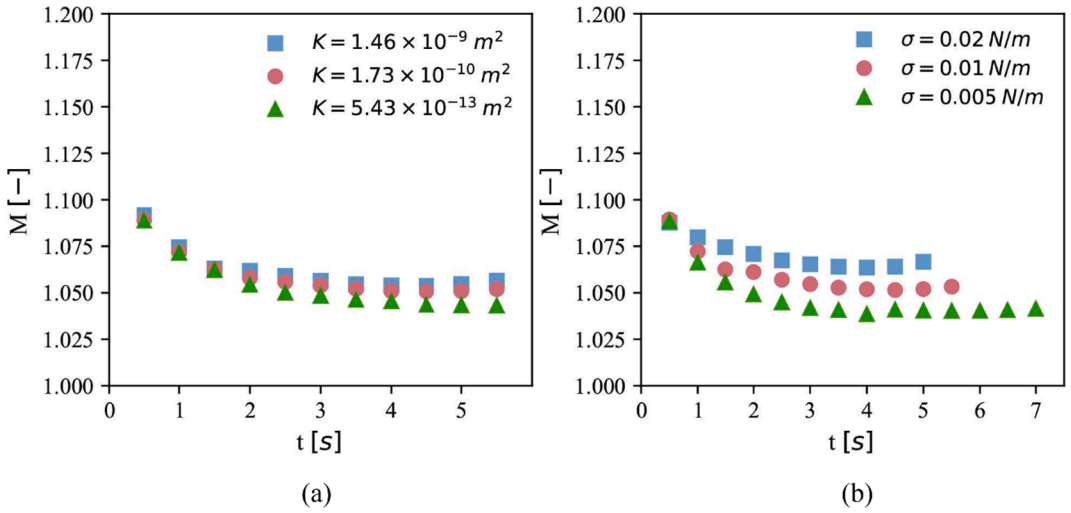

Fig. 10. Evolutions of the mobility with time for (a) various permeabilities and for (b) various surface tension coefficients. (For interpretation of the references to color in this figure legend, the reader is referred to the web version of this article.)

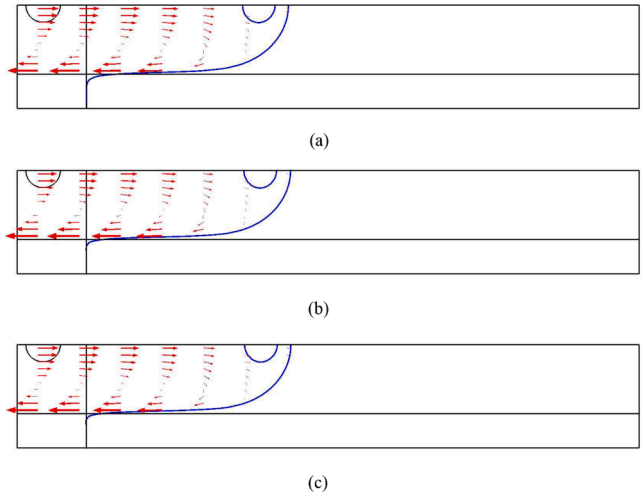

Fig. 11. Relative velocity vector profiles in the channel at $t = 1.8s$ for various tow permeabilities: (a) 1.46×10^{-9} m^2, (b) 1.73×10^{-10} m^2, (c) 5.43×10^{-13} m^2. (For interpretation of the references to color in this figure legend, the reader is referred to the web version of this article.)

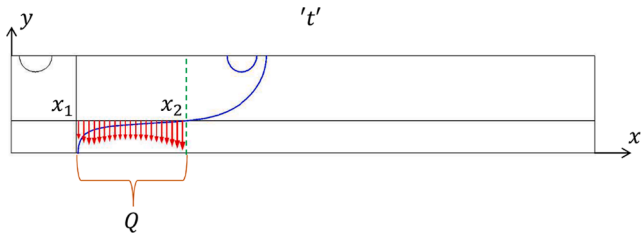

Fig. 12. Schematic description of the seepage flow into the porous media during the filling process. (For interpretation of the references to color in this figure legend, the reader is referred to the web version of this article.)

resin in the porous media is large compared to other cases, the advancement of the flow front in the channel is slower with a high permeability. At the same time, the void with a large permeability is found to be closer to the resin flow front, causing the void to escape from the resin earlier. In the case of very low permeability, e.g., $K = 5.43 \times 10^{-13}$ m^2 and $K = 5.43 \times 10^{-15}$ m^2, the flow fronts advance at the same speed, which implies that the effect of viscous dissipation within the porous media vanishes. The porous media behave like a no-slip wall, which is consistent with the result in the above void formation process; see Fig. 3(d) and (e). Fig. 9 shows the evolutions of the void and resin flow front at different time periods for various surface tension coefficients, e.g., $\sigma = 0.02$ N/m,$\sigma = 0.01$ N/m, and $\sigma = 0.005$ N/m, respectively. The void with largest surface tension coefficient (i.e., $\sigma = 0.02$ N/m) is observed to migrate slowest, and escape from the resin the earliest. This may be interpreted by the "bubble pushing effect", i.e., bubble with a high surface tension coefficient behaves like the rigid particle and it may push the fluid into the porous media for enhanced seepage flow, causing the advancement of flow front in the channel to be slower compared to other cases. Similar phenomena with rigid particles have been reported by Hwang et al. [34].

To quantitatively characterize the migration behavior of the void against the resin flow front, the void mobility is introduced, which is defined as the ratio of the void velocity to the resin flow front velocity

$$M = \frac{u_{\text{void}}}{u_{\text{resin}}}. \tag{21}$$

The symbols u_{void} and u_{resin} denote the velocity of the void and resin, respectively. Mobility greater than one ($M > 1$) indicates that the void migrates faster than the resin flow front, and thereby the void could escape from the resin; otherwise, it may be trapped in the resin. Fig. 10 shows the evolution of the mobility with time for various permeabilities (Fig. 10(a)) and for various surface tension coefficients (Fig. 10(b)). It can be observed that, in each case, the bubble mobility is always larger than one, which indicates faster bubble motion relative to the flow front, if the bubble is located near the centerline between porous media. However, as reported by Cubaud and Ho [35], for the bubbly flow (e.g., the liquid volume fraction close to one) in square microchannels, the bubble mobility is always less than one, which implies the bubble may be trapped in the liquid. The slip effect of the porous wall in the present work seems to be responsible for such an enhanced bubble mobility. Moreover, as the bubble approaches toward the flow front and particularly in close proximity of the interface, film drainage needs to occur to displace liquids toward the wall. This hydrodynamic drainage is usually slow and exerts a repulsive force against the bubble motion, which leads to reduction in the mobility in time (Fig. 10(a) and (b)). Additionally, the cases with larger permeabilities (Fig. 10(a)) and larger surface tension coefficients (Fig. 10(b)) yield higher bubble mobility. It may be because in these cases, the high permeable effect and "bubble pushing" effect lead to more resin wetting the fibers within the porous media,

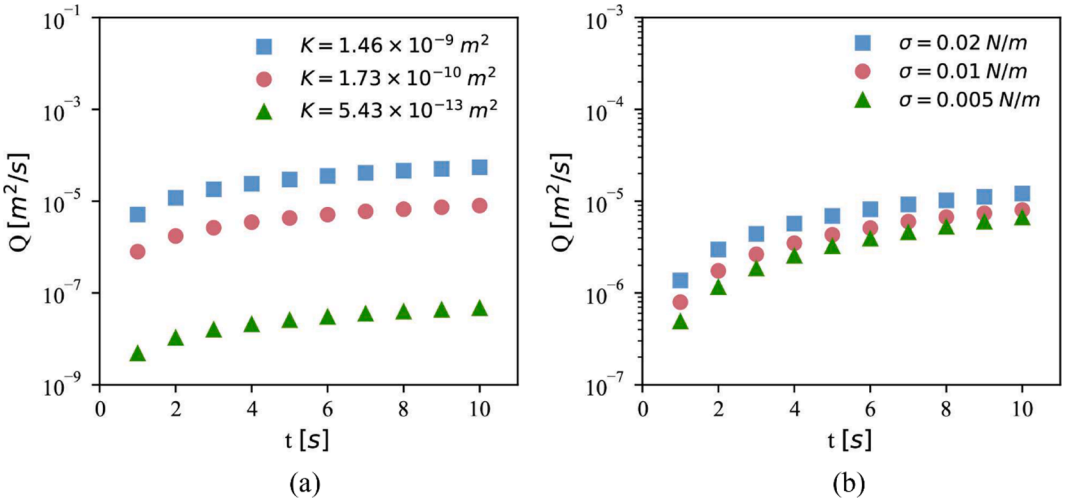

Fig. 13. Integrated seepage flow rates for (a) various permeabilities and (b) various surface tension coefficients. (For interpretation of the references to color in this figure legend, the reader is referred to the web version of this article.)

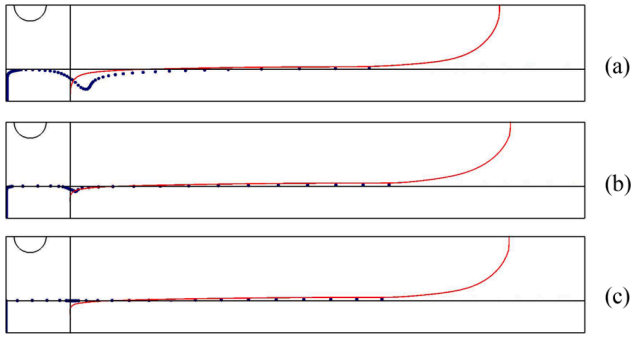

Fig. 14. Particle distribution as well as profiles of resin flow front at $t = 7.5s$, for various permeabilities: (a) 1.46×10^{-9} m^2, (b) 1.73×10^{-10} m^2, (c) 5.43×10^{-13} m^2. (For interpretation of the references to color in this figure legend, the reader is referred to the web version of this article.)

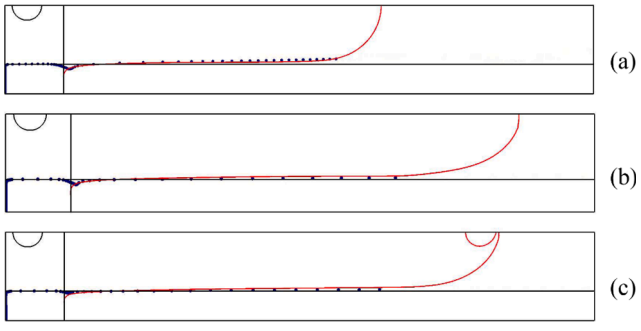

Fig. 15. Particle distribution as well as profiles of resin flow front at $t = 7.5s$, for various surface tension coefficients: (a) $\sigma = 0.02$ N/m, (b) $\sigma = 0.01$ N/m, (c) $\sigma = 0.005$ N/m. (For interpretation of the references to color in this figure legend, the reader is referred to the web version of this article.)

therefore the flow front in the channel moves slower compared to other cases. As for the effect of the surface tension (Fig. 10(b)), another possible mechanism might be slow film drainage with a large bubble deformation in case of a low interfacial tension. Low interfacial tension yields large deformation of a bubble near the flow front such that the area surrounding the drainage increases. This may lead to slower film drainage and a bubble motion might get slower as well, which seems to be responsible for the reduction in the mobility. Thus, voids in the cases subjected to larger permeability and higher surface tension coefficient could escape from the resin earlier, which is consistent with the results shown in Fig. 8 and Fig. 9. It is worthwhile to mention the work of Gangloff et al. [21] on the bubble transport in a parallel flow channel bounded by permeable walls for comparison. The mobility ranges from around 1.25 to 1.5 and the case with a higher permeable wall shows a lower mobility, which is opposite with what we have found in the present study. The reason for this discrepancy is not clear at the moment. It is probably due to non-optimal effective viscosity and related seepage flows. It needs further investigation.

The reason for enhanced mobility with the permeability can be interpreted with the presence of seepage flow through porous media and fountain flow effects. During the filling process, the resin flow in the channel is considered as a fountain flow [36]. Fig. 11 shows the profiles of relative velocity vector $((u - u_{front}, v)$, with u_{front} being the velocity at the flow front) in the channel for various tow permeabilities. One can observe that resin at the center of the channel migrates faster than that adjacent to the wall. The material at the flow front is pushed forward and 'fountains' to the channel wall. In the present case, the channel is bounded by a porous wall, which facilitates the resin starting adjacent to the flow front to penetrate through the porous wall, i.e., the formation of seepage flow. As shown in Fig. 12, at a certain time, the seepage flow rate can be obtained by integrating the vertical velocity component per unit width on the porous interface: i.e., $\int_{x_1}^{x_2} v dx$. Fig. 13 shows the integrated seepage flow rate for various permeabilities and surface tension coefficients as a function of time. It can be observed that the cases with larger permeabilities and larger surface tension coefficients yield a higher seepage flow rate, which indicates that more resin adjacent to the flow front in these cases propagates into the porous media, leading to low transport speed of the flow front; therefore, the voids can escape from the resin more easily and earlier.

To prove the presence of the seepage flow associated with the fountain flow, the particle tracing method has been applied. A large number of massless fluid particles are placed at the inlet of the channel and the migration of the particles is recorded to trace the flow of the resin. For a given time, the particle distribution within the channel along with the resin flow front for various permeabilities and for various surface tension coefficients are presented in Fig. 14 and Fig. 15, respectively. In each case, a large number of fluid particles are detected in the porous region, which verifies the presence of the seepage flow. Further, a considerable number of particles are found in the porous region in the cases of large permeability (Fig. 14(a)) and of large surface tension coefficient (Fig. 15(a)), indicating that much more resin flows

into the porous media, which is consistent with the above interpretation that the cases with large permeability (Fig. 13 (a)) and with large surface tension coefficient (Fig. 13 (b)) exhibit a higher seepage flow rate.

4. Conclusions

Stokes-Brinkman coupling with optimal parameters was applied to evaluate the void formation and transport in dual-scale fibrous porous media during the advanced composites processing. These optimal parameters, i.e., the effective viscosity in the continuous interfacial stress condition and stress jump coefficient in the stress jump condition, were accurately characterized. A series of multiphase simulations with the level-set method have been conducted to record the evolutions of the void formation and the void transport against with the flow front position of the resin. It was found that the void appears in cases with low tow permeabilities and small aspect ratios. Additionally, the tow distance between the two fiber tows seems to affect the number of voids formed. Voids immerged in the resin subjected to high permeability and large surface tension yielded large mobility values, which indicated that these voids can easily escape from the resin. Evidence from the particle tracing method reveals that in high permeability and large surface tension cases, more seepage flows are observed adjacent to the flow front owing to the fountain flow nature and the "bubble pushing effect", which indicates that the voids in these cases transported faster, and therefore, can easily escape from the resin.

CRediT authorship contribution statement

Jin Gang Lu: Formal analysis, Investigation, Writing – original draft. **Sang Bok Lee:** Conceptualization, Funding acquisition. **T. Staffan Lundström:** Conceptualization, Writing – review & editing. **Wook Ryol Hwang:** Supervision, Methodology, Writing – review & editing.

Declaration of Competing Interest

The authors declare that they have no known competing financial interests or personal relationships that could have appeared to influence the work reported in this paper.

Acknowledgements

The authors acknowledge financial supports from the National Research Foundation of Korea (NRF-2019R1A2C1003974 and 2020M3D1A208095121), "Kempestiftelserna" (The Kempe Foundations, www.kempe.com), and the Senior Talent Foundation of Jiangsu University (5501130016).

Data availability

The data that support the findings of this study are available from the corresponding author upon reasonable request.

Appendix A

In modeling the filling stage of Liquid Composites Molding (LCM) processes, the capillary effects have been often neglected, as the capillary pressure is usually much lower than the inlet resin pressure [37]. Nevertheless, when dealing with flows through the fabrics, which exhibits a dual-scale behavior, it is of great importance to include the capillary pressure, which affects the saturation of resin in the tow. In this regard, here we introduce a strategy to incorporate the equilibrium capillary pressure along the resin flow front inside a porous domain in the presence of the interfacial slip in our numerical framework. The stress jump due to the interfacial tension is often integrated into the momentum equation as an additional body force or the surface stress that are distributed over the neighborhood of the interface, when it is formulated within a Eulerian frame work such as the volume-of-fluid method [38] or the level-set method [39]. The former is usually called the continuous surface force (CSF) [40] and the latter is called the continuous surface stress. For the problem in the present study, one may introduce an additional distributed body force, $(p_{ca}\boldsymbol{n}\delta(\phi))$, with p_{ca} being the equilibrium capillary pressure around the resin-air interface inside porous media $(\partial\Omega_{\text{intf}} \cap \Omega_{\text{p}})$, to incorporate the capillary pressure contribution within a single momentum equation (Eq. (17) in the main text) with both the continuous and discontinuous interfacial stress condition (See also [30])

$$-\int_{\Omega} p(\nabla\cdot v)d\Omega + \int_{\Omega} 2\mu(\boldsymbol{D}(\boldsymbol{u}):\boldsymbol{D}(\boldsymbol{v}))d\Omega + \int_{\Omega} 2\lambda(\mu_e-\mu)(\boldsymbol{D}(\boldsymbol{u}):\boldsymbol{D}(\boldsymbol{v}))d\Omega + \int_{\Omega} -\lambda\frac{\mu}{K}\boldsymbol{u}\cdot\boldsymbol{v}d\Omega = -\sigma\int_{\Omega}\left(\left(\boldsymbol{I}-\left(\boldsymbol{n}\boldsymbol{n}^{T}\right)\right)\delta(\phi)\right) : \boldsymbol{D}(\boldsymbol{v})d\Omega + \int_{\partial\Omega_{\text{inlet}}} \Delta p(\boldsymbol{n}\cdot\boldsymbol{v})d\Gamma + \int_{\Omega_{\text{p}}} \lambda_{ca}(p-p_{ca})\boldsymbol{n}\delta(\phi)d\Omega. \tag{A1}$$

In Eq. (A1), the last term indicates a constraint for the distributed body force $p_{ca}\boldsymbol{n}\delta(\phi)$along the interface inside the porous media $\left(\partial\Omega_{\text{intf}} \cap \Omega_{\text{p}}\right)$ with the Lagrangian multipliers, which are defined over the porous domain $\lambda_{ca} \in L^2(\Omega_{\text{p}})$. Though the above weak form is complete in its form, it is not appropriate to directly implement Eq. (A1) within the current numerical framework, as a large number of the equation rows with the Lagrangian multipliers λ_{ca} outside the resin-air interface become singular. To correct this, we have added a naturally satisfied equation of the continuity as the augmented constraints to the weak form instead of the single last term in Eq. (A1):

$$\int_{\Omega_{\text{p}}} \lambda_{ca}(p-p_{ca})\varphi(\delta)\boldsymbol{n}\delta(\phi)d\Omega + \int_{\Omega_{\text{p}}} \lambda_{ca}(\nabla\cdot\boldsymbol{u}-\varepsilon)(1-\varphi(\delta))\boldsymbol{n}\delta(\phi)d\Omega, \tag{A2}$$

We choose the tolerance ε as 10^{-6} and the interface function $\varphi(\delta)$ is defined by one near the interface $\left(\left|H(\boldsymbol{x})-\frac{1}{2}\right| < \varepsilon\right)$ and by zero elsewhere, where the numerical Heaviside function was defined in Eq. (14) in the main text. By doing this, one can avoid singular row equations from the Lagrangian multipliers λ_{ca} outside the resin-air interface. We use the continuous linear interpolation for the Lagrangian multiplier λ_{ca}.

The capillary pressure refers to the pressure difference across the interface between immiscible fluids. It can be estimated using the Young-Laplace equation [41], i.e., $\Delta p = \sigma(1/R_1 + 1/R_2)$The symbols σ, R_1, R_2 denote the surface tension coefficient, the radii of curvature of interface between the immiscible fluids. Based on the Young-Laplace equation, Bayram and Powell [42] derived the expression of the capillary pressure with certain

geometric quantities and the equilibrium contact angle between the fibers resin: $p_{ca} = \sigma cos(\theta + \alpha_b)/(r(1 - cos\alpha_b) + d)$, with the symbols θ, r, d, and α_b being the contact angle, fiber radius, half of the gap distance between fibers, and directional body angle, respectively. For flows through the transverse tow, it is accepted that the resin flow front moves inward perpendicular to the fibers and thus the mean capillary pressure is used. According to Neacsu et al. [43], for the hexagonal packing structure of the fibers, the mean capillary pressure is

$$p_{ca} = (\sigma/r)\cdot\frac{\left[sin(\alpha_{sub} + \theta) - sin\left(\alpha_{inf} + \theta\right)\right]}{\left(\frac{5\pi}{6}(1+\eta) - 1 - \sqrt{3}/2\right)}, \tag{A3}$$

where $\eta = \sqrt{\pi/(2\sqrt{3}(1-\varepsilon_t))} - 1$, $\alpha_{sup} \approx (\pi/2 - \theta)$, $\alpha_{inf} \approx (\theta - \pi/2)$, and ε_t is the porosity. In the present work, the usage of the physical capillary pressure yields convergence issue during simulations. Therefore, we tested only the relative capillary pressure to the inlet pressure.

The effect of capillary pressure on the process of both the void formation and migration have been investigated, as shown in Figs. A1 and A2. Three different capillary pressure cases are considered: i.e., $p_{ca}/p_{inlet} = 0, -0.01$and -0.1, respectively. Detailed information of the boundary conditions can be found in the main text. For the void formation process, based on the evolutions of the resin flow front profile shown in Fig. A1, one can observe that, for very low capillary pressure cases (e.g., $p_{ca}/p_{inlet} = 0$and -0.01), the profiles of the resin flow front are almost overlapped from the beginning to the final state. In the case of a larger capillary pressure ($p_{ca}/p_{inlet} = -0.1$), as the saturation develops, the resin flow front impregnates faster than those subjected to low capillary pressures due to the capillary effects inside the porous region. At the same time, the resin profile in the channel advances slower than the other two cases, which in fact eliminate the difference of the saturation speed in the porous region and that in the pure fluid channel, making the shape of the resin flow front undistorted. The capillary effect was found to hinder the formation of the void from this simulation result.

For the bubble migration process, according to the profiles of the resin flow front (Fig. A2), one can observe that in the case of a larger capillary pressure ($p_{ca}/p_{inlet} = -0.1$), the bubble breaks up earlier. This may be caused by a higher seepage flow rate towards the porous region. It is of great interest that, at the early stage before the bubble breaks up, the resin flow front subjected to higher capillary pressure moves fastest, while at the final stage after the bubble breaks up, it yields a slowest migration speed. Details of effects of the capillary pressure in the presence of the slip should be investigated through extensive simulations in the future.

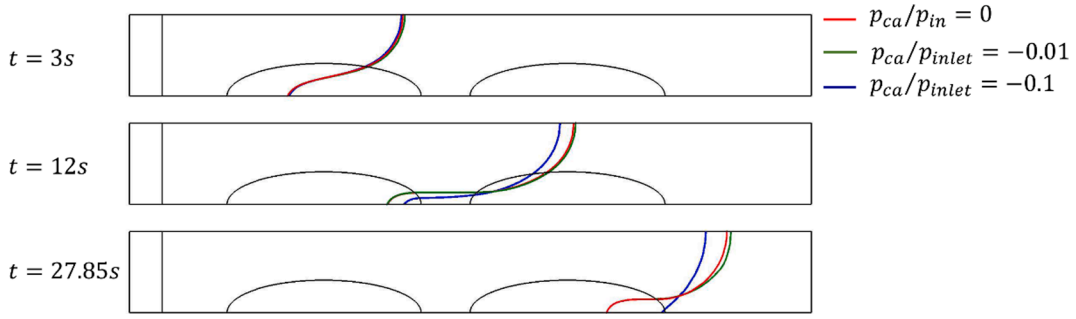

Fig. A1. The profiles of resin flow front ($\phi = 0.5$) at different stages for various capillary pressures. The permeability in this case is$K = 1.73 \times 10^{-10}$ m^2.

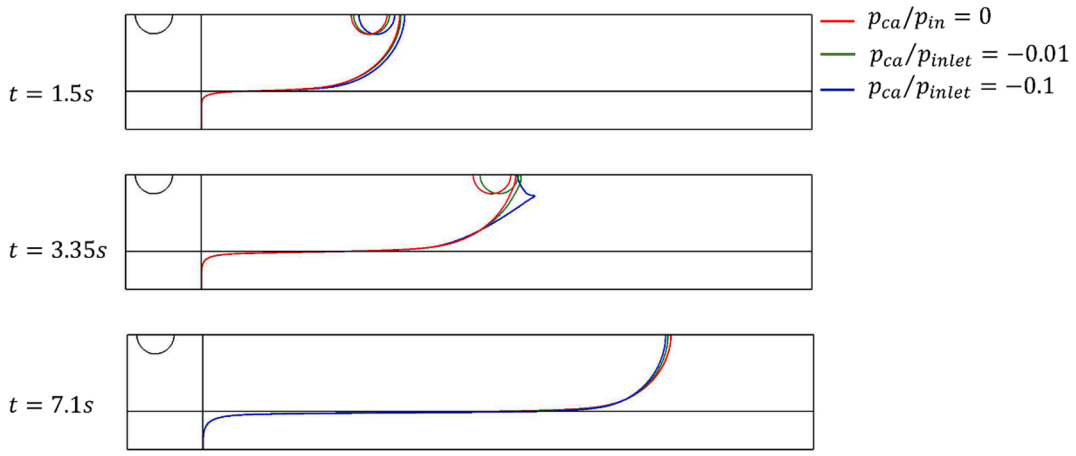

Fig. A2. Void evolutions as well as profiles of resin flow front at different moments for various capillary pressures. The permeability in this case is$K = 1.46 \times 10^{-9}$ m^2. (For interpretation of the references to color in this figure legend, the reader is referred to the web version of this article.)

References

[1] Leclerc JS, Ruiz E. Porosity reduction using optimized flow velocity in Resin Transfer Molding. Compos Part A Appl Sci Manuf 2008;39(12):1859–68.
[2] Dimitrovová Z, Advani SG. Mesolevel analysis of the transition region formation and evolution during the liquid composite molding process. Comput Struct 2004; 82(17-19):1333–47.
[3] Yang B, Bi FY, Wang SL, Ma C, Wang SB, Li S. Modeling meso-scale-void formation during through-thickness flow in liquid composite molding. Express Polym Lett 2020;14(1):77–89.
[4] Aaboud B, Bizet L, Saouab A, Nawab Y. Effect of the spatial variation of permeability on air bubble creation and compression. J Reinf Plast Compos 2020; 39(7-8):285–98.
[5] Dimitrovová Z, Advani SG. Free boundary viscous flows at micro and mesolevel during liquid composites moulding process. Int J Numer Meth Fluids 2004;46(4): 435–55.
[6] Aaboud B, Saouab A, Park CH. Modeling of air bubble dynamics during resin transfer molding by pore doublet model. Int J Adv Manuf Technol 2019;105(5-6): 2343–55.
[7] Vilà J, Sket F, Wilde F, Requena G, González C, LLorca J. An in situ investigation of microscopic infusion and void transport during vacuum-assisted infiltration by means of X-ray computed tomography. Compos Sci Technol 2015;119:12–9.
[8] Park Chung Hae, Woo Lee. Modeling void formation and unsaturated flow in liquid composite molding processes: a survey and review. J Reinf Plast Compos 2011;30 (11):957–77.
[9] Patiño Iván David, Power Henry, Nieto-Londoño César, Flórez Whady Felipe. Stokes-Brinkman formulation for prediction of void formation in dual-scale fibrous reinforcements: a BEM/DR-BEM simulation. Comput Mech 2017;59(4):555–77.
[10] Jinlian Hu, Yi Liu, Xueming Shao. Study on void formation in multi-layer woven fabrics. Compos Part A Appl Sci Manuf 2004;35(5):595–603.
[11] Frishfelds Vilnis, Lundström T Staffan, Jakovics Andris. Bubble motion through non-crimp fabrics during composites manufacturing. Compos Part A Appl Sci Manuf 2008;39(2):243–51.
[12] Abdelwahed Mohamed Amine Ben, Wielhorski Yanneck, Bizet Laurent, Bréard Joël. Bubble formation and transport in T-junction for application to Liquid Composite Molding: Wetting effect. J Compos Mater 2014;48(1):37–48.
[13] Schell JSU, Deleglise M, Binetruy C, Krawczak P, Ermanni P. Numerical prediction and experimental characterisation of meso-scale-voids in liquid composite moulding. Compos Part A Appl Sci Manuf 2007;38(12):2460–70.
[14] Lundström T Staffan, Gebart B Rikard. Influence from process parameters on void formation in resin transfer molding. Polym Compos 1994;15(1):25–33.
[15] Shih Chih-Hsin, Lee L James. Analysis of void removal in liquid composite molding using microflow models. Polym Compos 2002;23(1):120–31.
[16] Gourichon B, Binetruy C, Krawczak P. A new numerical procedure to predict dynamic void content in liquid composite molding. Compos Part A Appl Sci Manuf 2006;37(11):1961–9.
[17] Kang Kai, Koelling Kurt. Void transport in resin transfer molding. Polym Compos 2004;25(4):417–32.
[18] Lundström T Staffan. Measurement of void collapse during resin transfer moulding. Compos A Appl Sci Manuf 1997;28(3):201–14.
[19] DeValve C, Pitchumani R. Simulation of void formation in liquid composite molding processes. Compos Part A Appl Sci Manuf 2013;51:22–32.
[20] Yang Junying, Jia Yuxi, Sun Sheng, Ma Dongjun, Shi Tongfei, An Lijia. Mesoscopic simulation of the impregnating process of unidirectional fibrous preform in resin transfer molding. Mater Sci Eng, A 2006;435-436:515–20.
[21] Gangloff John J, Hwang Wook R, Advani Suresh G. Characterization of bubble mobility in channel flow with fibrous porous media walls. Int J Multiph Flow 2014; 60:76–86.
[22] Gangloff John J, Hwang Wook R, Advani Suresh G. The investigation of bubble mobility in channel flow with wavy porous media walls. Int J Multiph Flow 2015; 70:1–14.
[23] Patiño Arcila Iván, Power Henry, Nieto Londoño César, Flórez Escobar Whady. Boundary Element Method for the dynamic evolution of intra-tow voids in dual-scale fibrous reinforcements using a Stokes-Darcy formulation. Eng Anal Bound Elem 2018;87:133–52.
[24] Lu JG, Woo NS, Hwang WR. The optimal Stokes-Brinkman coupling for two-dimensional transverse flows in dual-scale fibrous porous media using the effective Navier slip approach. Phys Fluids 2019;31(7):073108.
[25] Bakshi A, Altantzis C, Bershanska A, Stark AK, Ghoniem AF. On the limitations of 2D CFD for thin-rectangular fluidized bed simulations. Powder Technol 2018;332: 114–9.
[26] Ochoa-Tapia J Alberto, Whitaker Stephen. Momentum transfer at the boundary between a porous medium and a homogeneous fluid—II. Comparison with experiment. Int J Heat Mass Transf 1995;38(14):2647–55.
[27] Lu Jingang, Jang Hye Kyeong, Lee Sang Bok, Hwang Wook Ryol. Characterization on the anisotropic slip for flows over unidirectional fibrous porous media for advanced composites manufacturing. Compos A Appl Sci Manuf 2017;100:9–19.
[28] Lu Jin Gang, Cho Seung Chan, Hwang Wook Ryol. On the Interfacial Flow Over Porous Media Composed of Packed Spheres: Part 1-Identification of the Effective Slip Length. Transp Porous Media 2020;133(1):139–57.
[29] Lu Jin Gang, Hwang Wook Ryol. On the interfacial flow over porous media composed of packed spheres: part 2-optimal Stokes-Brinkman coupling with effective Navier-Slip approach. Transp Porous Media 2020;132(2):405–21.
[30] Hwang Wook Ryol, Advani Suresh G. Numerical simulations of Stokes-Brinkman equations for permeability prediction of dual scale fibrous porous media. Phys Fluids 2010;22(11):113101. https://doi.org/10.1063/1.3484273.
[31] Frishfelds V, Lundström TS, Jakovics A. Lattice gas analysis of liquid front in non-crimp fabrics. Transp Porous Media 2010;84(1):75–93.
[32] Lafaurie Bruno, Nardone Carlo, Scardovelli Ruben, Zaleski Stéphane, Zanetti Gianluigi. Modelling merging and fragmentation in multiphase flows with SURFER. J Comput Phys 1994;113(1):134–47.
[33] Gebart BR. Permeability of unidirectional reinforcements for RTM. J Compos Mater 1992;26(8):1100–33.
[34] Hwang Wook Ryol, Advani Suresh G, Walsh Shawn. Direct simulations of particle deposition and filtration in dual-scale porous media. Compos A Appl Sci Manuf 2011;42(10):1344–52.
[35] Cubaud Thomas, Ho Chih-Ming. Transport of bubbles in square microchannels. Phys Fluids 2004;16(12):4575–85.
[36] Papathanasiou TD, Ogadhoh SO, Ingber MS. Microstructure evolution during injection molding of particulate composites. Int Polym Proc 1995:184–96.
[37] Lawrence Jeffrey M, Neacsu Valentin, Advani Suresh G. Modeling the impact of capillary pressure and air entrapment on fiber tow saturation during resin infusion in LCM. Compos A Appl Sci Manuf 2009;40(8):1053–64.
[38] Renardy M, Renardy Y, Li J. Numerical simulation of moving contact line problems using a volume-of-fluid method. J Comput Phys 2001;171(1):243–63.
[39] Sethian JA, Smereka P. Level set methods for fluid interfaces. Annu Rev Fluid Mech 2003;35:341–72.
[40] Chang YC, Hou YT, Merriman B, Osher S. A level-set formulation of Eulerian interface capturing methods for incompressible fluid flows. J Comput Phys 1996; 124(2):449–64.
[41] De Gennes P-G, Brochard-Wyart F, Quere D. Capillarity and Wetting Phenomena: Drops, Bubbles, Pearls, Waves. New York: Springer; 2004.
[42] Bayramli E, Powell RL. The normal (transverse) impregnation of liquids into axially oriented fiber bundles. J Colloid Interface Sci 1990;138(2):346–53.
[43] Neacsu V, Abu Obaid A, Advani SG. Spontaneous radial capillary impregnation across a bank of alignedmicro-cylinders. Part I: theory and model development. Int J Multiph Flow 2006;32(6):661–76.